catalysts

MDPI

Article

Metal Ions (Li, Mg, Zn, Ce) Doped into La_2O_3 Nanorod for Boosting Catalytic Oxidative Coupling of Methane

Jing Xiong, Hongbin Yu, Yuechang Wei *, Chengshu Xie, Kezhen Lai, Zhen Zhao and Jian Liu

State Key Laboratory of Heavy Oil Processing, College of Science, China University of Petroleum, Beijing 102249, China; xiongjing@cup.edu.cn (J.X.); 18810896989@163.com (H.Y.); xiechengshu6@163.com (C.X.); laikezhen0207@163.com (K.L.); zhenzhao@cup.edu.cn (Z.Z.); liujian@cup.edu.cn (J.L.)

* Correspondence: weiyc@cup.edu.cn

Abstract: A series of La_2O_3 nanorod catalysts with doping of active metal ions (Li, Mg, Zn and Ce) were synthesized successfully by the hydrothermal method. The La_2O_3 nanorods show a uniform size with the length of 50–200 nm and the width of 5–20 nm, and the {110} crystal facet is a preferentially exposed surface. The active metal ions (Li, Mg, Zn and Ce) doped into the lattice of La_2O_3 nanorods enhance the selectivity of the desired products during oxidative coupling of methane (OCM) and decrease the reaction temperature. Among these catalysts, the Mg-La_2O_3 catalyst exhibits the best catalytic performance during the OCM reaction, i.e., its selectivity and yield of C2 products at 780 °C is 73% and 21%, respectively. The effect of doped metal ions on catalytic activity for OCM was systematically investigated. Insight into the fabrication strategy and promoting factors of the OCM reaction indicates the potential to further design a high-efficient catalyst in the future.

Keywords: La_2O_3 nanorod; metal ions; doping effect; OCM reaction; selectivity

Citation: Xiong, J.; Yu, H.; Wei, Y.; Xie, C.; Lai, K.; Zhao, Z.; Liu, J. Metal Ions (Li, Mg, Zn, Ce) Doped into La_2O_3 Nanorod for Boosting Catalytic Oxidative Coupling of Methane. *Catalysts* **2022**, *12*, 713. https://doi.org/10.3390/catal12070713

Academic Editors: Zongjian Liu and Jun Li

Received: 4 June 2022
Accepted: 27 June 2022
Published: 29 June 2022

1. Introduction

Low-carbon hydrocarbons, such as ethylene and propylene, are important high-value-added basic chemical raw materials, which are applied widely to produce chemical products (plastics, fibers and rubbers) [1]. The technical routes of low-carbon olefins that originated from naphtha resources are increasingly limited by the depletion of oil resources. Thus, there is a severe demand to exploit and develop the route of synthesizing low-carbon olefins from non-petroleum resources for ensuring the efficient utilization of natural energy and resources. With the large commercial development of shale gas, the catalytic conversion of CH_4 (main composition of shale gas) into low-carbon olefins is a very promising technical route, which can be divided into the indirect and direct routes [2]. The indirect pathway (CH_4 –› syngas –› low carbon olefin) with long processes needs high energy and feed consumption [3]. The oxidative coupling of methane (OCM) with oxygen into low-carbon olefins is an ideal route to achieve the direct conversion [4,5]. However, it is difficult to find the catalyst of high efficiency to achieve the high CH_4 conversion into low-carbon olefins.

A series of high-efficient catalysts for the OCM reaction have been designed and fabricated, such as Na-W-Mn oxides [6,7], Li-MgO [8], ABO_3 perovskite-type oxides [9], rare earth oxides [10] and so on [11–13]. Among the catalysts, Na-W-Mn-based catalysts have high catalytic performance during the OCM reaction process, and its yield of ethane and ethylene (C2) products can reach nearly 25% [14]. However, efficient catalytic performances usually need a high reaction temperature (>800 °C), which is accompanied with high energy consumption during the reaction [15,16]. For Li-MgO catalysts, they have also exhibited outstanding catalytic performance during the OCM reaction, but their catalytic stability was limited by the sintering and volatilization of the surface active Li component [17]. It is worth noting that the rare earth oxide catalysts have high catalytic activity for the OCM reaction at relatively low temperatures [18]. For example, La-based oxide with nanorod

morphology showed high catalytic activity for OCM and even under low temperature conditions of 450 °C [2]. Thus, it is hopeful that the La-nanorod oxide will further improve catalytic performance for the OCM reaction. Among the typical alkaline earth metal, transition metal and rare earth metal, the elements with suitable oxidation capacity were chosen to test the oxidative coupling performance. The preferentially exposed {110} facet possesses lower atomic density, which reduces the amount of medium-strength basic sites (La^{3+}–O^{2-} pairs). The introduction of metal ions can further adjust the number of surface oxygen species. Therefore, the catalysts with appropriate surface oxygen species possess suitable oxidation ability to improve C2 selectivity and avoid the deep oxidation.

The understanding of the catalytic mechanism is the top priority to research OCM catalysts. The processes of the OCM reaction consist of two parts, heterogeneous and homogeneous reaction [19]. The heterogeneous reaction process includes adsorption and activation steps of gaseous CH_4 and O_2, and the C–H bond of CH_4 is activated and broken. Four carbon-containing species (CH_3, CH_2, CH, C) would form during the C–H break processes. These carbon-containing species adsorbed on reaction sites can generate carbon-containing compounds by couple reactions or reacting with surface O species to form oxygen-containing hydrocarbons (alcohols, aldehydes, ketones, acids, etc.), carbon deposition, CO and CO_2. The homogeneous reaction process includes the coupling of various carbon-containing free radicals separated from the surface of catalyst to generate hydrocarbons (alkanes, alkenes, alkynes, etc.), or the reaction of carbon-containing free radicals with O_2 to generate CO and CO_2 products [20]. Multi-carbon alkanes are adsorbed and activated on the surface of catalyst, and then undergo a dehydrogenation (oxidation or oxygen-free) reaction to generate the olefins. For example, the $CH_3\cdot$ formed on the surface of the catalyst is desorbed and coupled into C_2H_6, and it is further adsorbed and dehydrogenated to produce C_2H_4. C_2H_4 is the secondary product of the ethane dehydrogenation reaction, which is an important reaction pathway in the OCM process. In addition, the by-products can be further introduced into C–C coupling to form carbon-containing compounds. Thus, the degrees of C–H bond dissociation and C–C bond coupling are the key controlling factors for enhancing single-pass yield of the OCM reaction [21,22]. In addition, the surface alkaline is usually related to the generation of C2 products [23]. There is a demand to improve the surface alkaline density of the catalysts for CH_4 conversion into target products. Metal oxide components can act as the active center for the OCM reaction catalyst [24,25]. By introducing low-valent ions into the lattice of La_2O_3, the oxygen vacancies and surface alkaline density can affect the charge distribution in oxide, which results in promoting the formation of C2 products. [26,27] Thus, the selectivity for C2 products could be improved, and the performance of OCM reaction would be enhanced.

Herein, a series of the catalysts of metal ions (Li, Mg, Zn, Ce) doped into La_2O_3 nanorods were prepared by the hydrothermal method, which are abbreviated as X-La_2O_3 (Li-La_2O_3, Mg-La_2O_3, Zn-La_2O_3 and Ce-La_2O_3). The surface of X-La_2O_3 catalysts preferred the exposed {110} crystal facet, which has a loose atomic arrangement and is beneficial to the activation of the reactant gases (CH_4 and O_2) [28]. The doping of metal ions into La_2O_3 nanorod can remarkably enhance the catalytic performance of OCM, and the doped metal ions into the La_2O_3{110} facet are crucial for C2 production. Among the catalysts, the Mg-La_2O_3 catalyst has the best catalytic performance for the OCM reaction. The catalytic mechanism of X-La_2O_3 catalysts for OCM was proposed. The understanding of controlling the catalytic cleavage of C–H bonds is beneficial for further developing high-performance OCM catalysts.

2. Results and Discussions

2.1. XRD Patterns

The crystal structures of the La_2O_3 and X-La_2O_3 catalysts were correlated with the catalytic activity of OCM. To confirm the formation and phase structure of the La_2O_3 and X-La_2O_3 catalysts, the XRD patterns are shown in Figure 1. The Bragg diffraction peaks (2θ) located at 20–60° can be matched to the (100), (002), (102), (110), (103) and (112) face

of the La_2O_3 nanorod. The XRD diffraction peaks of all the catalysts are matched with the hexagonal phase of La_2O_3 by referring to the standard PDF card (PDF# 05-0602). In addition, the diffraction peaks centered at 44.5° are $La_2O_2CO_3$ (JCPDS 84-1963), which is assigned to the hexagonal phase structure. It is attributed to the transformation of La_2O_3 to $La_2O_2CO_3$ partially during the calcination processes, which can improve the ability to resist carbon deposition. In the process of the high-temperature reaction, $La_2O_2CO_3$ will react with carbon on the surface to form La_2O_3 if trace carbon deposition is produced. It is worth noting that, after the introduction of doped metal ions, the XRD patterns of X-La_2O_3 catalysts are identical to that of the La_2O_3 nanorod. The characteristic diffraction peaks in the catalysts are matched with the La_2O_3 phase, while the characteristic diffraction peaks assigned to the doped metal ions are not observed. It indicates that the metal ions (Li, Mg, Zn, Ce) can be doped into the lattice of the La_2O_3 nanorod, and they have high dispersion on the surface of the La_2O_3{110} facet at the atomic scale via the one-pot hydrothermal method. The Debye–Scherrer equation was used to calculate the average crystallite sizes (*D*) of the La_2O_3 nanorod, which is estimated using the half-height width of (104) the diffraction peak of the La_2O_3 nanorod, [29] and the results are shown in Table 1. After the introduction of doped metals ions into the La_2O_3 nanorod, the sizes of crystallite have not obviously changed. It suggests that the structure of the X-La_2O_3 catalysts is well maintained.

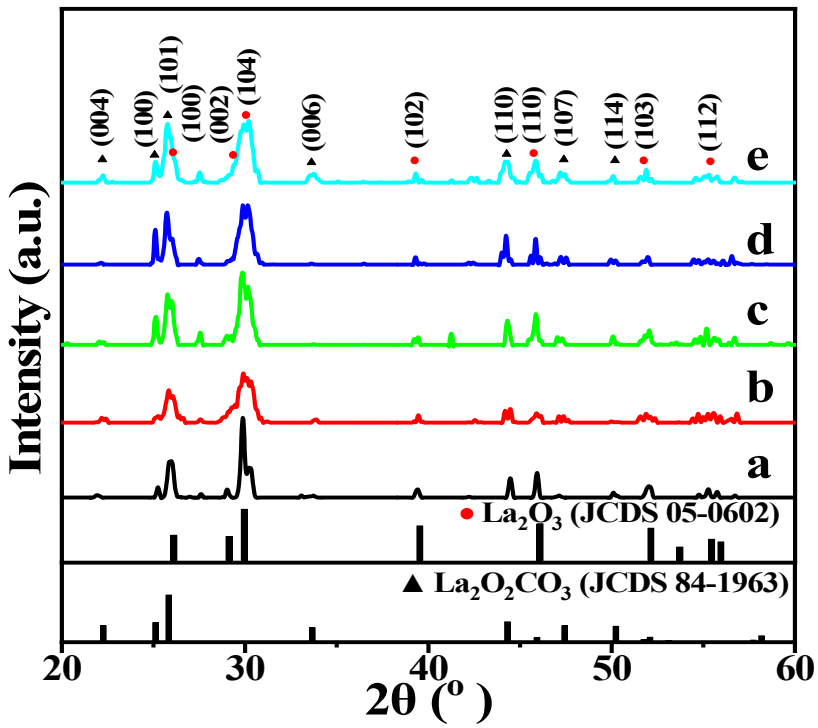

Figure 1. XRD pattern of the La_2O_3 and X-La_2O_3 catalysts. (**a**) La_2O_3; (**b**) Li-La_2O_3; (**c**) Mg-La_2O_3; (**d**) Zn-La_2O_3; (**e**) Ce-La_2O_3.

Table 1. BET surface area, pore size, supported nanoparticle size of pure La_2O_3 and X-La_2O_3 catalysts.

Sample	$S_{BET}/m^2 \cdot g^{-1}$	D_p/nm	Vp $/cm^3 \cdot c^{-1}$	D_{SEM} /nm	L_{SEM}/nm
La_2O_3	37	8.6	0.12	10 ± 5	150 ± 20
Li-La_2O_3	35	9	0.14	10 ± 5	150 ± 20
Mg-La_2O_3	32	9.2	0.16	10 ± 5	150 ± 20
Zn-La_2O_3	33	8.8	0.13	10 ± 5	150 ± 20
Ce-La_2O_3	36	8.3	0.11	10 ± 5	150 ± 20

2.2. Raman Spectra

The UV-Raman spectra are used to further investigate the surface crystal structures of La_2O_3, Li-La_2O_3, Mg-La_2O_3, Zn-La_2O_3 and Ce-La_2O_3 catalysts; the results are shown in Figure 2. The Raman shifts that appeared at 289, 349 and 459 cm^{-1} are assigned to the La-O lattice vibration of the hexagonal La_2O_3 phase, and the Raman shift at 1073 cm^{-1} is attributed to the surface CO_3^{2-} species, which is in accord with XRD. After the introduction of doped metal ions, there is no obvious difference in the four main Raman peaks. It suggests that the effect of doping metal ions on the phase structure of the hexagonal La_2O_3 nanorod can be negligible. However, it is worth noting that for the Mg-La_2O_3 and Ce-La_2O_3 catalysts, there is one new Raman peak centered at 372 cm^{-1}, which is assigned to the formation of carbonate species on the surface of the catalysts. The Raman peak centered at 1073 cm^{-1} also blue shifts to 1088 cm^{-1} and the height has clearly increased. It indicates that the doped Mg and Ce ions into La_2O_3 is beneficial to CO_2 adsorption. [30,31] It is crucial to boost the generation of surface CO_3^{2-} species during the catalytic OCM reaction [32]. Thus, the Mg-La_2O_3 catalyst has potential to promote the catalytic performance for the OCM reaction.

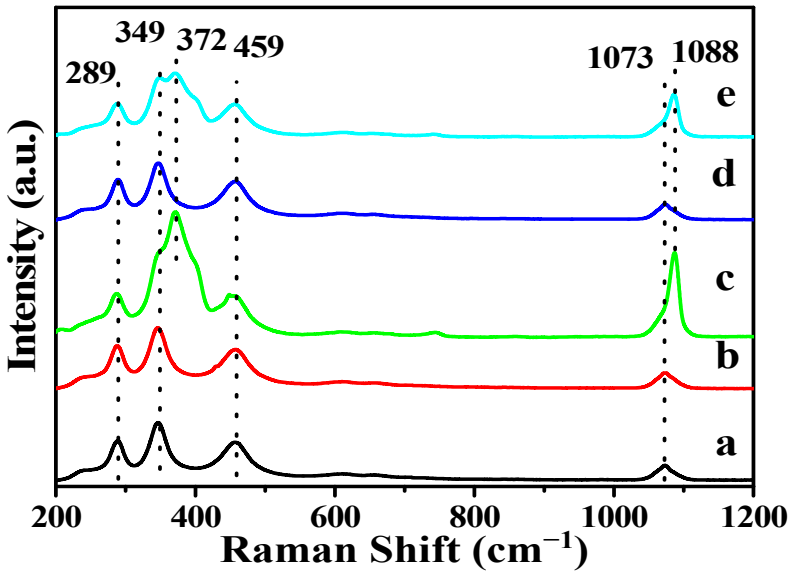

Figure 2. Raman spectra of the La_2O_3 and X-La_2O_3 catalysts. (**a**) La_2O_3; (**b**) Li-La_2O_3; (**c**) Mg-La_2O_3; (**d**) Zn-La_2O_3; (**e**) Ce-La_2O_3.

2.3. SEM Images

Figure 3 shows the SEM images of the $La(OH)_3$, La_2O_3 and X-La_2O_3 catalysts. As shown in Figure 3a, the $La(OH)_3$ nanorods synthesized by the hydrothermal method show the diameter of 5–20 nm and the length of 50–200 nm. The SEM images of La_2O_3 nanorods obtained by the calculation are shown in Figure 3b. The La_2O_3 sample shows the perfect nanorod morphology, which is similar with the before calcined $La(OH)_3$. It suggests that the dehydration process of $La(OH)_3$ at 800 °C in air has not damaged its nanorod structure. The SEM images of the X-La_2O_3 catalysts with the same doping amount of 2 wt% are further shown in Figure 3c–f. After the introduction of doped metal ions (Li, Mg, Zn, Ce), the nanorod-shaped structure of the X-La_2O_3 catalysts is maintained, indicating that the nanorod structure of La_2O_3 has high thermal stability, and the doped metal ions have no effect on the shape structure of the La_2O_3 nanorod. The uniform nanorod structure of the catalysts is beneficial to investigate the role of doped metal ions in X-La_2O_3 catalysts during the catalytic OCM reaction.

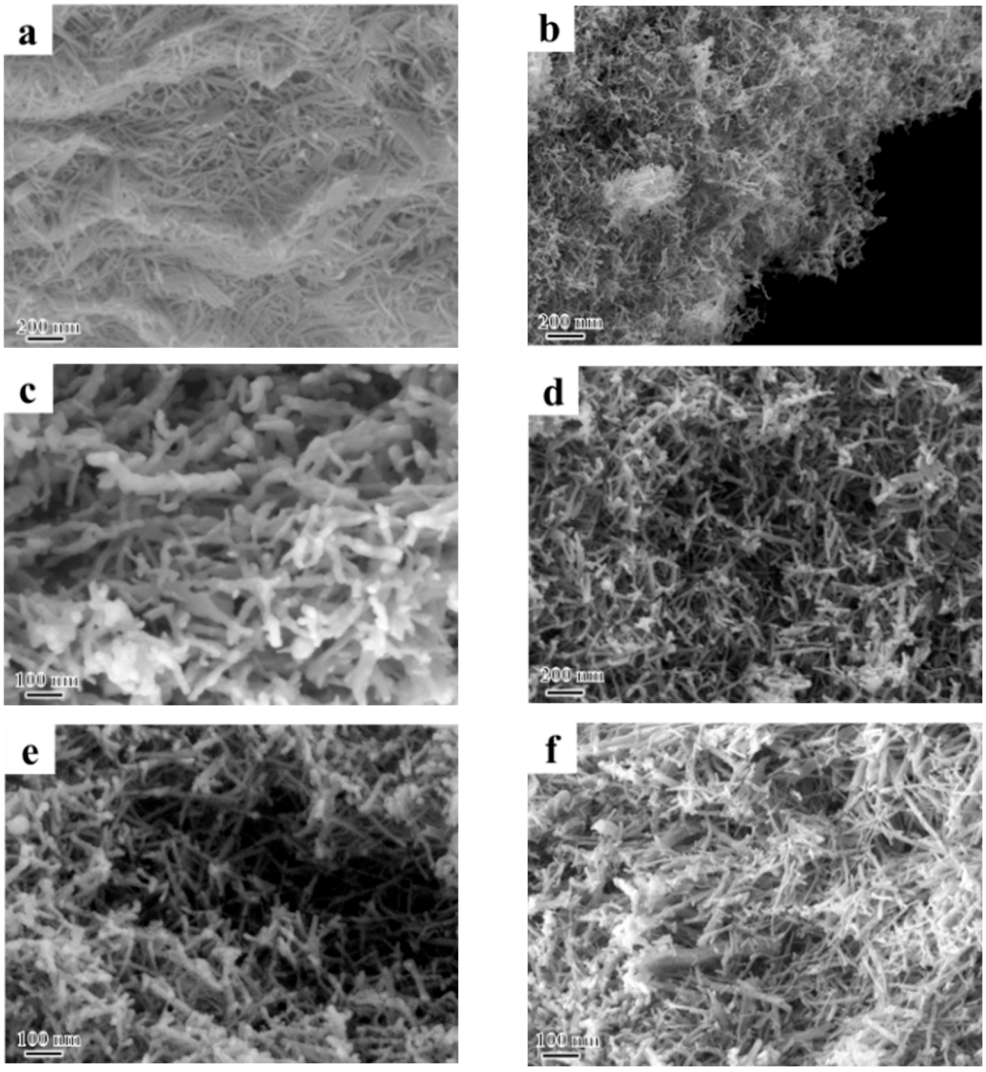

Figure 3. SEM images of the $La(OH)_3$, La_2O_3 and X-La_2O_3 catalysts. (**a**) $La(OH)_3$; (**b**) La_2O_3; (**c**) Li-La_2O_3; (**d**) Mg-La_2O_3; (**e**) Zn-La_2O_3; (**f**) Ce-La_2O_3.

2.4. TEM Images

The TEM technology is used to further investigate the microstructures of the catalysts, and the TEM images of pure La_2O_3 and typical Mg-La_2O_3 catalysts are shown in Figure 4. As shown in Figure 4a, the La_2O_3 sample shows uniform nanorod morphology. It is in accord with the SEM image with the diameter of 5–20 nm and length of 50–200 nm. The HRTEM image of the La_2O_3 sample shown in Figure 4b is used to further study the crystal structure. One La_2O_3 nanorod shows the clear lattice fringes, and its interplanar crystal spacing is 0.20 nm, which corresponds to the characteristic lattice fringe width of {110} crystal facets. It suggests that the main exposed crystal facets of the La_2O_3 nanorod are {110} crystal facets. It has been found that the {110} crystal facets of the La_2O_3 nanorod with low surface density of exposed La atoms are an active surface for the activation of reaction gases [1]. Therefore, the selectively exposed active {110} crystal facets would enhance catalytic performance of OCM reaction. After the introduction of doped metal ions (Li, Mg, Zn, Ce), the Mg-La_2O_3 catalyst shows the perfect nanorod-shaped structure in Figure 4c, indicating that the doping of metal ions has not affected the structure of the La_2O_3 nanorod. As shown in Figure 4d, the Mg-La_2O_3 catalyst exhibits the clearly lattice atoms of the La element, while the doped Mg atoms have not been observed, suggesting that Mg ions show single atomic dispersion into the lattice of the La_2O_3 nanorod. The images of other catalysts

with doped metal ions are shown in Figure S4. The elemental analyses of catalysts were further demonstrated by the HAADF-STEMEDS mapping, and the results are shown in Figure 5. The yellow regions indicate the dispersion of La elements, and the red regions indicate the dispersion of O elements. The orange, purple and green regions are assigned to the dispersion of Mg, Zn and Ce elements, respectively. It is clearly revealed the existence and distribution of doped metal ions, La and O elements over the surface of La-based oxide nanorods. All the elements overlap at the same part, indicating that the dispersion of doped metal ions is highly uniform on the surface of La_2O_3. It is direct evidence to confirm the existence of doped metal ions in X-La_2O_3 catalysts. The doped metal atoms show single atomic dispersion into the lattice of the La_2O_3 nanorod. It is conducive to investigate the role of atomic metal sites on the surface of the La_2O_3{110} facet during the catalytic OCM reaction.

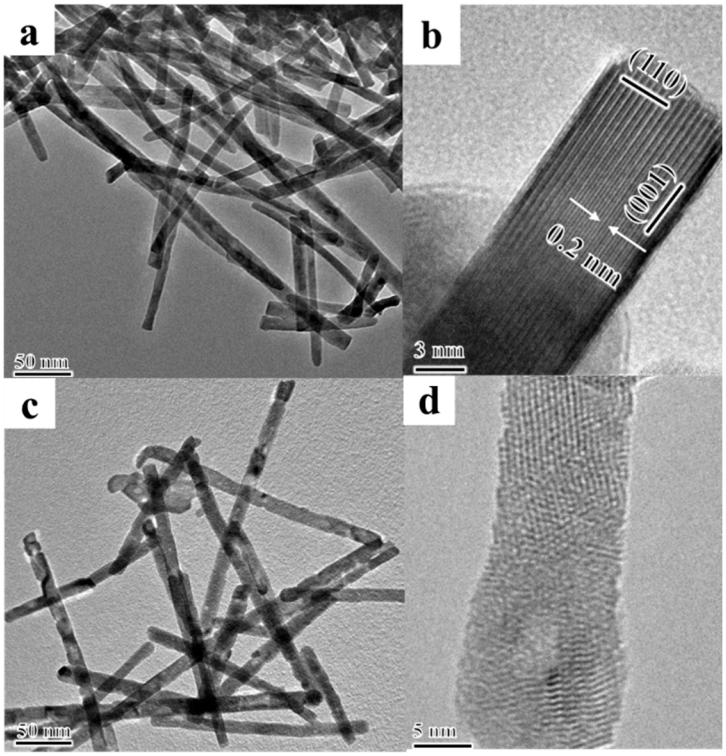

Figure 4. TEM and HRTEM images of pure La_2O_3 (**a**,**b**) and Mg-La_2O_3 (**c**,**d**) catalysts.

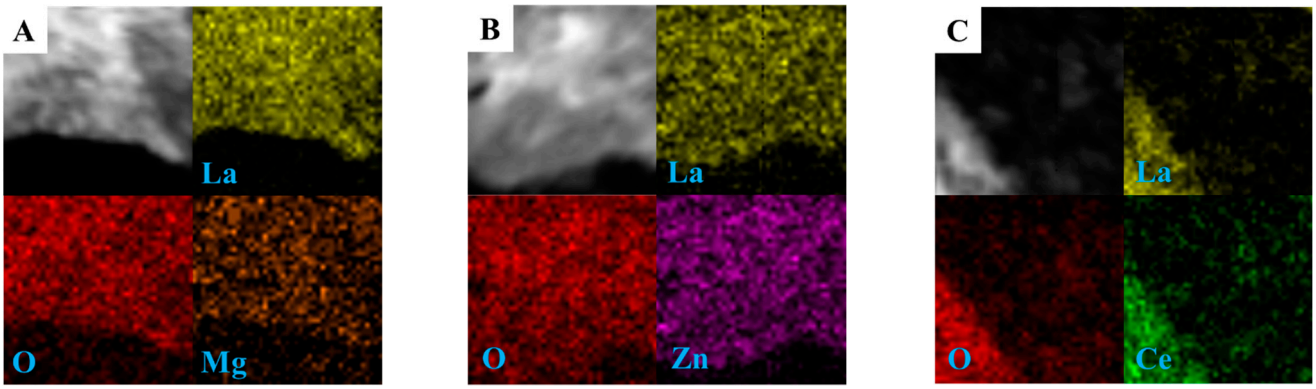

Figure 5. HR-STEM image and HAADF-STEM-EDX element-mapping analyses of La (yellow), O (red), Mg (orange), Zn (purple), Ce (green), (**A**) Mg-La_2O_3, (**B**) Zn-La_2O_3, (**C**) Ce-La_2O_3.

2.5. H_2-TPR Profiles

Figure 6 shows the H_2-TPR profiles of the catalysts to test their redox property. The H_2-TPR profile of the La_2O_3 catalyst has not consumed H_2 at 300–800 °C, indicating that the La_2O_3 nanorods have a poor redox property [33,34]. After the introduction of doped metal ions (Li, Mg, Zn and Ce), the X-La_2O_3 catalysts exhibited two peaks of H_2 consumption at 300–800 °C, indicating that the doped metal ions can promote the redox property of catalysts. For X-La_2O_3 catalysts, one H_2 consumption peak was observed at a low reduction temperature (470–580 °C), which is assigned to the reduction of the doped metal oxides or active oxygen species of catalysts located at the X-La_2O_3 interfaces [35]. Compared with the Li-La_2O_3 and Ce-La_2O_3 catalysts, the reduction peaks of Mg-La_2O_3 and Zn-La_2O_3 catalysts shift to near ~460 °C, and its proportion also decreases slightly. Among the doped catalysts, the lowest reduction temperature of the Mg-La_2O_3 catalyst is at 461 °C. In addition, the X-La_2O_3 catalysts show one reduction peak at 650–740 °C, which is attributed to the reduction of the lattice oxygen species originated from the doping of metal ions into the La_2O_3 nanorod. The doping of metal ions can promote the formation of strong-bonded X-O-La active sites between the metal ions and {110} crystal facets of La_2O_3 nanorods [36]. Thus, X-La_2O_3 catalysts provide high redox ability, suggesting good performance for the OCM reaction.

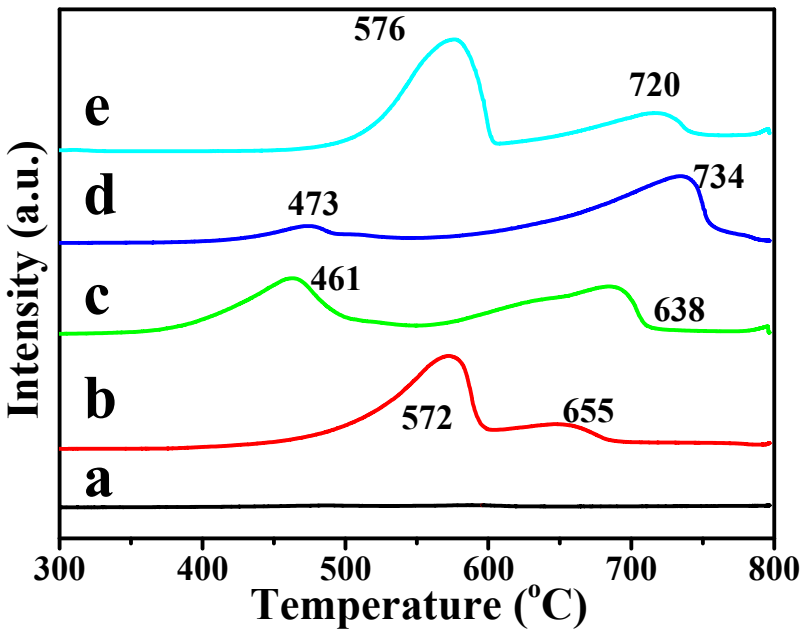

Figure 6. H_2-TPR profiles of the La_2O_3 and X-La_2O_3 catalysts. (**a**) La_2O_3; (**b**) Li-La_2O_3; (**c**) Mg-La_2O_3; (**d**) Zn-La_2O_3; (**e**) Ce-La_2O_3.

2.6. N_2 Adsorption-Desorption Results

The N_2 adsorption-desorption experiment is used to test the pore size characteristics and the surface condition of the catalyst. The results of all catalysts are shown in Figure S5. All the catalysts exhibited IV-type N_2 adsorption–desorption curve and H3 type hysteresis loop. The relative pressure is 0.8–1 (P/P0). After introduction of the doped metal ions into La_2O_3, the X-La_2O_3 catalysts are consistent with the La_2O_3 catalyst, indicating that the surface areas of X-La_2O_3 catalysts have not been influenced by the doping of metal ions. In addition, as shown in Table 1, there is no obvious change in the specific surface area (30–40 $m^2 \cdot g^{-1}$) and pore volume (0.11–0.16 $cm^3 \cdot g^{-1}$) of all the catalysts. It indicates that the doping of metal ions cannot affect the morphology and surface microstructure of La_2O_3 nanorods.

2.7. XPS Results

To further study the surface element compositions and valence states of the catalysts, XPS was used to characterize the situation. The results of XPS have great correlation with the performance of the catalyst. The XPS peaks of La species in La_2O_3-based catalysts can be divided into $La3d_{3/2}$ and $La3d_{5/2}$ regions. As shown in Figure 7A, the XPS pattern of $La3d_{3/2}$ in the pure La_2O_3 nanorod has one main peak with binding energy at 849.8 eV and one satellite peak with binding energy at 853.8 eV. In addition, the $La3d_{5/2}$ spectra show one main peak with binding energy at 833.2 eV and one satellite peak with binding energy at 835.1 eV, which is assigned to the La^{3+} species. It indicates the formation of pure La_2O_3 phase in the as-prepared samples.

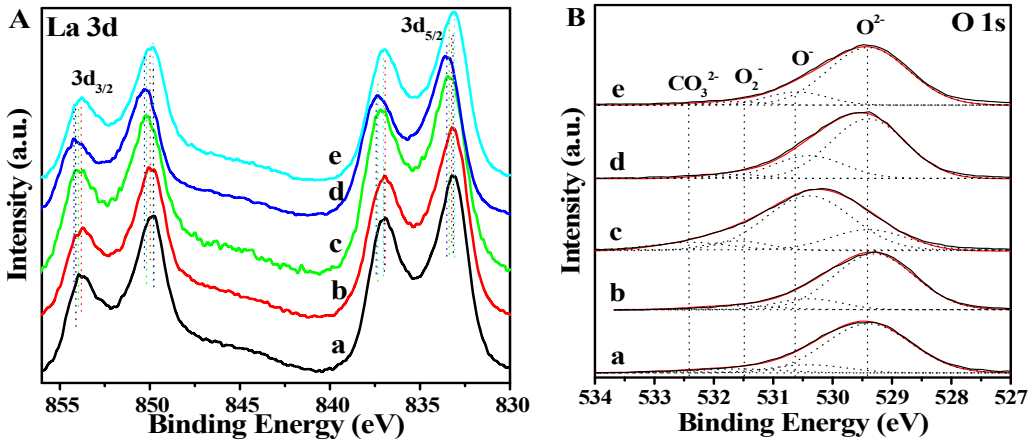

Figure 7. XPS spectra of La3d (**A**) and O1s (**B**) over the La_2O_3 and X-La_2O_3 catalysts. (**a**) La_2O_3; (**b**) Li-La_2O_3; (**c**) Mg-La_2O_3; (**d**) Zn-La_2O_3; (**e**) Ce-La_2O_3.

After the introduction of doped metal ions, the peak position migrates to high binding energy. For the Li-La_2O_3 catalyst, the binding energy of $La3d_{5/2}$ slightly shifts to a higher binding energy at 833.3 eV, which is attributed to the La–O–Li bond vibration between Li and La_2O_3. [37–39] In addition, the positions of XPS peaks over Mg-La_2O_3 and Zn-La_2O_3 catalysts have obviously shifted. The binding energy of $La3d_{5/2}$ over the Mg-La_2O_3 catalyst migrated to 833.5 eV, and the binding energy of $La3d_{3/2}$ of Mg-La_2O_3 catalyst also slightly changed (850.2 eV) in comparison with the pure La_2O_3 sample (849.8 eV). It indicates that the Mg ion is doped into the lattice of La_2O_3, and there is an electron transfer from Mg atoms to La atoms [40]. Based on the XPS peak positions of the Mg-La_2O_3 catalyst, it suggests that Li^+, Mg^{2+}, Zn^{2+}, and Ce^{4+} ions would enter into the lattice gap of La_2O_3, and the replace sites of the lanthanum ions lead to a large number of electrophilic surface oxygen species [41]. For the Zn-La_2O_3 catalyst, the XPS peak of the La element is similar with that of the Mg-La_2O_3 catalyst. The La3d XPS peaks of the Ce-La_2O_3 catalyst have no obvious change compared with that of pure La_2O_3. The result may be attributed to the fact that that the Ce nucleus has a similar atomic radius with the La atom, and the binding of electrons is uniform, so that the binding energy does not change significantly.

In order to further study the active oxygen species of X-La_2O_3 catalysts, the XPS profile of O1s is shown in Figure 7B. The four different types of oxygen species in the catalysts constitute the asymmetric O1s spectra [22]. The binding energies at 529.4, 530.6, 531.6 and 532.4 eV are attributed to the lattice oxygen species (O^{2-}), chemisorbed oxygen species (O_2^-), surface oxygen species (O_2^{2-}/O^-) and oxygen-containing contaminant (CO_3^{2-}), respectively. The proportions of oxygen species are shown in Table 2. Combined with the catalytic performances of the catalyst, the surface oxygen species in the catalyst are related to the selectivity of the catalyst [42,43]. After the introduction of doped metal ions (Mg and Zn), the surface oxygen contents of Mg-La_2O_3 and Zn-La_2O_3 catalysts are obviously higher than the other catalyst. The order of the surface oxygen content values is

as follows: Mg-La_2O_3 (63) > Zn-La_2O_3 (25) > Li -La_2O_3 (13) > Ce-La_2O_3 (13) > La_2O_3 (12). It suggests that doping metals can effectively improve the chemical environment of oxygen species in the La_2O_3 catalyst. Thus, the doped metal ions in the La_2O_3 nanorods should bear a positive charge, indicating that doping metals can effectively improve the chemical environment of oxygen species in the La_2O_3 catalyst. For example, the doped Mg cation into the La_2O_3 {110} surface will induce the electron transfer, which involves Mg atoms into Mg^{2+} ions. The excess electrons will be distributed throughout the whole catalyst, which is less favorable to the localized state. The positive charge of the surface Mg cation on the Mg-La_2O_3 catalyst is conducive to improve the capability of adsorption and activation for gaseous oxygen, which is helpful for the formation of surface oxygen species. In addition, the surface alkalinity of the catalyst is also beneficial to the selectivity of the catalyst, [44] and the content of CO_3^{2-} can indicate the surface alkalinity of the catalyst. The Mg-La_2O_3 catalyst has the highest carbonate content, which has the potential to improve the selectivity of the catalyst for the OCM reaction. The binding energy of doped metal ions are shown in Figure S6, indicating that the active metal is well doped into the La_2O_3 nanorod. To obtain accurate binding energy, the binding energy of C1s was used to make corrections in Figure S7.

Table 2. Surface compositions and oxidation states O species over X-La_2O_3 catalysts derived from XPS analyses.

Catalysts	O Species (%)			
	O^{2-}	O_2^-	CO_3^{2-}	O^-/O_2^{2-}
La_2O_3	80	6.9	1.5	12
Li-La_2O_3	81	5.2	0.4	13
Mg-La_2O_3	21	7.9	7.9	63
Zn-La_2O_3	71	3.2	1.1	25
Ce-La_2O_3	83	3.1	1.3	13

2.8. Catalytic Performances

Figure 8 shows the catalytic performances of La_2O_3 and X-La_2O_3 catalysts for the OCM reaction at 500 to 800 °C. The FID detector records the C2 products (ethane and ethylene) and the gas chromatograph provides the amounts. The data error of the measured CH_4 conversion and C2 selectivity is within 1.0 and 2.0%, respectively. As shown in Figure 8A, the CH_4 conversion rate of pure La_2O_3 is highest with the Li-La_2O_3, Mg-La_2O_3, Zn-La_2O_3 and Ce-La_2O_3 catalysts. After the introduction of active doped metals, the excess oxidation of CH_4 over the catalysts decreases significantly, indicating that the doping of metal ions affects the activation of CH_4 and reduces the conversion of CH_4. The La_2O_3 catalyst shows the highest CH_4 conversion rate (45%), while the catalyst with other doped metal ions is only close to 30%. It is well known that the OCM reaction takes place at a high temperature, and the chemisorbed oxygen species can oxidize CH_4 directly to CO_2. Based on the catalytic performances for the OCM reaction, it is revealed that the catalysts of metal ion (Li, Mg, Zn, Ce) doped La_2O_3 nanorods exhibit a lower CH_4 conversion than the pure La_2O_3 catalyst, while their catalytic selectivity for C2 products evidently increases. It is attributed to the fact that that the exposed {110} facet of the La_2O_3 nanorod possesses lower atomic density, and the introduction of doped metal ions can further adjust the content surface oxygen species. Thus, the catalysts with appropriate surface oxygen species can improve the C2 selectivity and avoid deep oxidation. The activation of C–H in the CH_4 molecule is the rate-controlling step of the OCM reaction. The catalytic selectivity of the catalyst determines methyl radicals, which quickly coupled to produce light olefins (from deep oxidation). With the introduction of doped metal ions into the La_2O_3 lattice, the active oxygen species can promote the dissociation of the C–H bond. With the increase in the temperature (>700 °C), the CH_4 conversion increases significantly. Unfortunately, the high CH_4 conversion alone is not representative of the high catalytic performance of the catalyst. The deep oxidation of

CH_4 is a major problem [45]. Lowering the temperature for the OCM reaction is not only to reduce energy consumption, but also to improve the utilization ratio of the products [46].

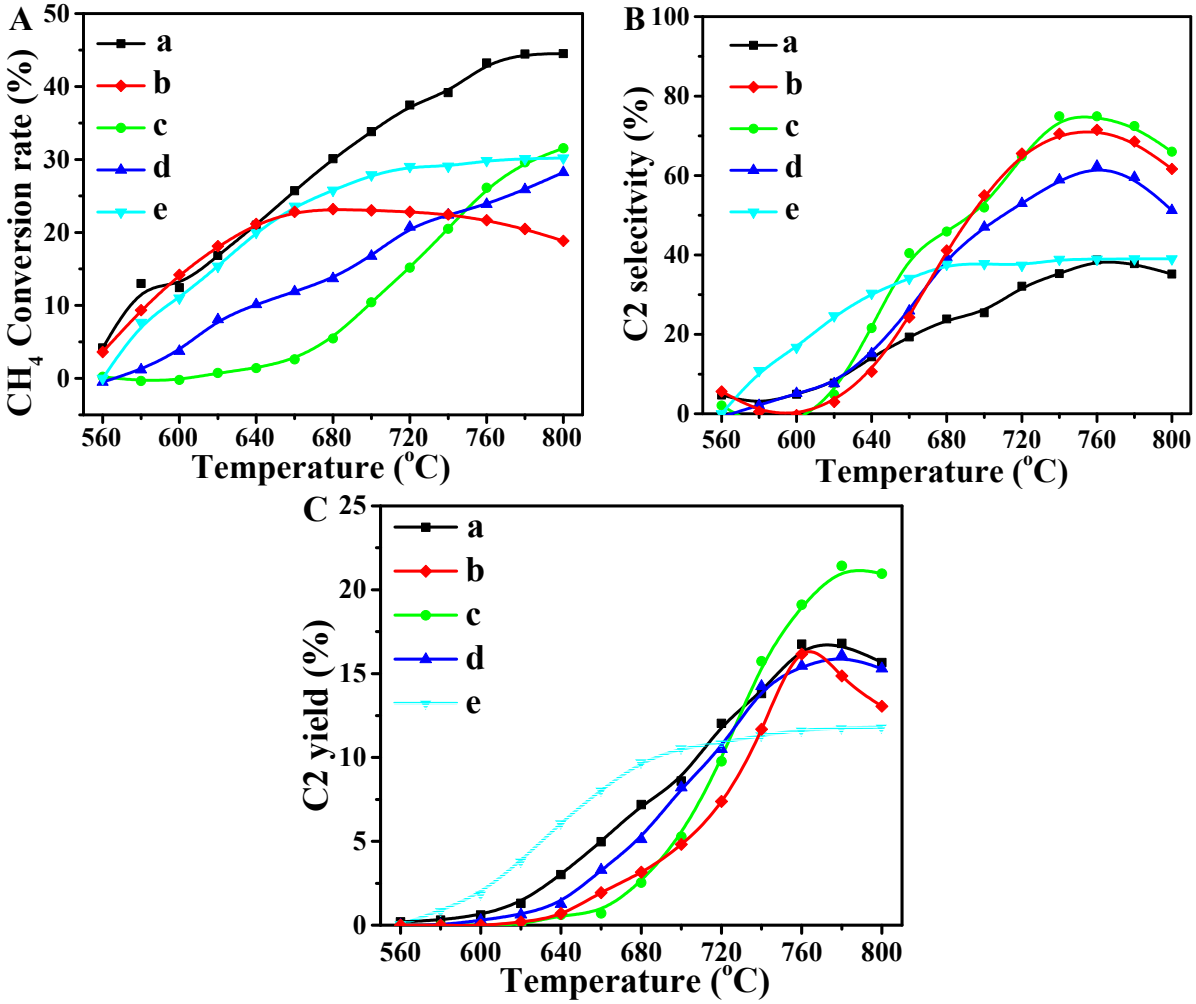

Figure 8. Catalyst conversion (**A**), selectivity (**B**) and yield (**C**) of C2 products over the La_2O_3 and X-La_2O_3 catalysts. (**a**) La_2O_3; (**b**) Li-La_2O_3; (**c**) Mg-La_2O_3; (**d**) Zn-La_2O_3; (**e**) Ce-La_2O_3.

The catalytic selectivity of C2 products (ethane and ethylene) over the catalysts for OCM was investigated at temperatures ranging from 500 to 800 °C, and the results are shown in Figure 8B. With the increase in the reaction temperature, the selectivity of the C2 products first increases and then decreases, and it reaches the maximum at 760 °C, indicating that the temperature is the optimum reaction condition for the catalytic OCM reaction, and the higher temperature can decrease the performance of the catalysts. If the temperature is decreased again, the CH_4 conversion and the selectivity of C2 products will be restored. The pure La_2O_3 catalyst shows relatively low selectivity of C2 products, i.e., its value is just 30%. Thus, although the pure La_2O_3 catalyst has high CH_4 conversion, its selectivity of C2 products is low, which is attributed to its lack of redox properties demonstrated by H_2-TPR. The CH_4 over the La_2O_3 catalyst is deep oxidized to CO_2 and CO, rather than producing the target product with C–C bond coupling [47]. Thus, the selectivity of pure La_2O_3 is remarkably lower than that of other catalysts.

Among the prepared catalysts, the Mg-La_2O_3 catalyst exhibits excellent selectivity for the OCM reaction, which is related to the promotion effect of doped Mg ions. The Mg-La_2O_3 catalyst requires higher temperatures to improve the catalytic performance for OCM. At the temperature range <700 °C, the selectivity of C2 products over the Mg-La_2O_3 catalyst is low and the main products are CO_2 and CO. With the increase in the

temperature (>700 °C), its catalytic performance for OCM increases very rapidly, and the maximum selectivity of C2 products (78.4%) over the Mg-La_2O_3 catalyst is obtained at 760 °C. Combined with the results of XPS, it is revealed that the chemisorbed oxygen species (O_2^-) lead to deep oxidation with CH_4, and surface oxygen species (O_2^{2-}/O^-) improve coupling of the C–C bond. Thus, the active sites for the absorption and conversion of CH_4 and O_2 will change with the introduction of doped metal ions, and they can be affected by the reaction temperature. The catalytic performances of all the catalysts for the OCM reaction decrease with the increase in temperature (>760 °C). [48,49] It is also noted that the Ce-La_2O_3 catalyst shows high the selectivity of C2 products at relatively low temperatures (<650 °C). La_2O_3 combined with the Ce component can markedly improve catalytic performance of the OCM reaction, which is better than that of the pure phase of La_2O_3. It is suggested that there are many active oxygen species that exist in the Ce-La_2O_3 catalyst. The active oxygen species is helpful to boost catalytic performance for the OCM reaction at low temperatures. With the increase in the temperature (>680 °C), the performance of the Ce-La_2O_3 catalyst for the OCM reaction has not decreased, suggesting that the Ce-La_2O_3 catalyst has higher stability than that of other catalysts.

The yields of C2 products are obtained by the product of conversion and selectivity at the same temperature, which is one of the most important evaluation indicators during the catalytic OCM reaction. One blank test (no catalyst) was performed on the blank tube loaded with quartz sand, and it was observed that the CH_4 conversion is close to 0%, and C2 products were not obtained in the range of 500–800 °C, indicating that the conversion of CH_4 to C2 products is dependent on the presence of the catalyst. Figure 8C exhibits the yields of C2 products over the La_2O_3 and X-La_2O_3 catalysts. Among the prepared catalysts, the Mg-La_2O_3 catalyst shows the largest yields of C2 products during the OCM reaction, and its value at 780 °C is 21%. In Table 3, the yields of C2 products over the Mg-La_2O_3 catalyst at 760 °C is 19% during the catalytic OCM reaction. As shown in Figure 8C, the ignition temperature of C2 yield over all the catalysts is 620 °C, and the catalytic performances are improved with the rising temperature. The maximum C2 yield of the other catalysts was close to 18% (pure La_2O_3, Li-La_2O_3 and Zn-La_2O_3), which is lower than that of the Mg-La_2O_3 catalyst. However, it is worth noting that at relatively low temperatures, the Ce-La_2O_3 catalyst shows the largest yields of C2 products during the OCM reaction. For example, the C2 yield at 680 °C is approximately 10%, which is in accord with the results of H_2-TPR. It indicates that the doping of metal ions into the La_2O_3 nanorod can enhance the catalytic performance for the OCM reaction, especially for boosting the selectivity and yield of C2 products [50,51]. Although the yields of the desired products over X-La_2O_3 catalysts are similar with that of the La_2O_3 catalyst, the consumption amounts of CH_4 decrease obviously because of the high selectivity of the desired products, which improve the utilization efficiency of CH_4 molecules and avoid the waste of CH_4 molecules caused by deep oxidation reactions [52]. It is crucial to improve the economic efficiency of the OCM reaction in practice.

Table 3. Catalytic Performances of X-La_2O_3 for OCM (T: 760 °C; C2: ethane and ethylene).

Catalyst	Conversion %	C2 Selectivity %	C2 Yield %
La_2O_3	43	39	17
Li-La_2O_3	22	67	15
Mg-La_2O_3	25	78	19
Zn-La_2O_3	23	62	14
Ce-La_2O_3	29	39	11

The stability of the catalysts is also important during the OCM reaction. The catalysts were further examined under the conditions of the OCM experiments for 15 h at 760 °C, and the results are shown in Figure S8. The Mg-La_2O_3 catalyst had good activity during 15 h of the OCM tests, and its CH_4 conversion, C2 selectivity, and yield values were almost unchanged. It indicates that the Mg-La_2O_3 catalyst has high catalytic stability during the

OCM reaction. In addition, the SEM and TEM images of the Mg-La_2O_3 catalyst used for 15 h during the OCM reaction are shown in Figures S9 and S10, respectively. It is noted that the nanorod structure of the Mg-La_2O_3 catalyst is perfect kept, indicating that the catalyst has high thermal stability.

The reaction mechanism OCM over nanorod X-La_2O_3 catalysts can be shown in Figure 9. La_2O_3 nanorods with exposed {110} crystal facets and doped metal can boost the active oxygen amounts by improving adsorption and activation for O_2 molecules. Oxygen vacancies derive from electron transfer from metal to La_2O_3. The activation of the C–H bond in methane was regarded as the rate-determining step in the OCM reactions, and the efficient formation and protection of $CH_3\cdot$ intermediates (from excessive oxidation) are largely determined by the catalytic selectivity to hydrocarbon products. In addition, with the introduction of metal components in the La_2O_3 lattice, the active oxygen species form to promote the hydrogen adsorption, as well as methane dissociation.

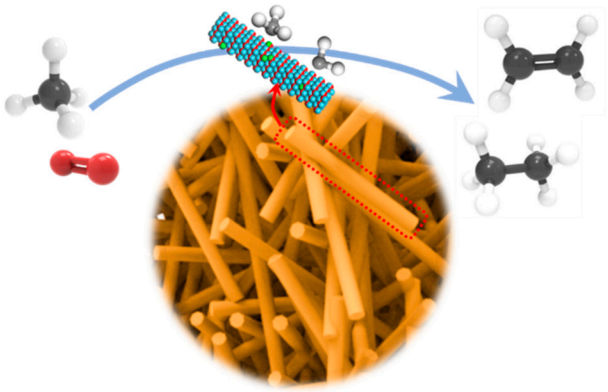

Figure 9. The reaction mechanism OCM over nanorod X-La_2O_3 catalysts.

2.9. Discussion on the Effect of Doped Metal Ions

The catalytic OCM reaction involves the two reactants of CH_4 and O_2. The performance of the catalysts for OCM are dependent on the activation property for CH_4 and O_2 reactants, which is affected by the crystal facets and active oxygen species compositions of the catalysts. Combined with the results of XRD, TEM and catalytic performances, the catalysts with high-proportioned {110} crystal facets have high catalytic conversion rates of CH_4, indicating that they can efficiently activate CH_4. The {110} facet of the La_2O_3 nanorods has high energy because of the variations in the basic properties. The La^{3+} cation in the hexagonal structure of La_2O_3 is encircled by five oxygen atoms, and the {110} facets comprise few O and La atoms compared with other crystal facets. Thus, the atomic arrangement density of the {110} crystal plane is lower than other crystal planes. The selectivity of La_2O_3 nanorods for CH_4 conversion to C2 products is lower than 40% in the range of 500–800 °C. To further improve the selectivity for C2 products, the surface activity elements (Li, Mg, Zn and Ce) are doped into the lattice of La_2O_3 nanorods. The catalytic selectivity of the X-La_2O_3 for OCM is better than that of the pure La_2O_3. The doping of metal ions show high dispersion into the lattice of La_2O_3 and do not affect the nanorod structure. With the introduction of the doped metal ions, the redox property of the X-La_2O_3 catalysts is clearly enhances, as determined by H_2-TPR, especially at the low temperatures. It is attributed to the formation of oxygen-anion vacancies induced by the metal ions doped into the lattice of La_2O_3. As a partial oxidation reaction, the active oxygen species should participate in the coupling of C–C bonds by the activation of the C–H bond to produce methyl radicals. Thus, the surface activity oxygen species are related to the catalytic performance for OCM reaction.

Based on the results of XPS, the doping of low-valence metal ions (Li^+, Mg^{2+}, Zn^{2+}) into the La_2O_3 nanorod can promote the formation of oxygen vacancy to keep the charge balance of X-La_2O_3 systems, while the doping effect of high-valence metal ions (Ce^{3+} or

Ce^{4+}) on the surface element states can be ignored. The Mg-La_2O_3 catalyst shows the largest surface ratio value of surface oxygen species, which is attributed to enhancing the mobility of lattice oxygen with exposed {110} crystal facets. Based on the results of O1s XPS, there are two kinds of oxygen species over the La-based catalysts, including O_2^- and O_2^{2-}, and the surface intensity of oxygen species will change with the introduction of metal ions (Li, Mg, Zn, Ce) doped into the La_2O_3 nanorod. The chemisorbed oxygen (O_2^-) and surface oxygen (O_2^{2-}/O^-) species play different roles in the reaction process. From the results of the catalytic performances for OCM, it is noted that the doping of metal ions can improve the selectivity for C2 products. Figure S11 shows the selectivity of X-La_2O_3 catalysts for CH_4 conversion to C2 products at 760 °C. Among the catalysts, the Mg-La_2O_3 catalyst shows the largest selectivity for CH_4 conversion to C2 products, i.e., its value at 760 °C is 78.4%, which is larger than that of pure La_2O_3 nanorods (36.7%). It is also found that the Mg-La_2O_3 catalyst exhibits the lowest conversion of CH_4, indicating that the doping of Mg ions can restrain the CH_4 conversion into CO and CO_2, and boost the coupling of C–C bonds, which results in the largest yield (21%) of C2 products at 780 °C. Combined with the results of XPS and their catalytic performances for the OCM reaction, it is revealed that the chemisorbed oxygen species (O_2^-) lead to deep oxidation with CH_4, and the surface oxygen species (O_2^{2-}/O^-) can improve coupling of the C–C bond. Thus, the CH_4 conversion over the catalysts of metal ions (Li, Mg, Zn, Ce) doped La_2O_3 nanorods is lower compared with pure La_2O_3 with the relatively higher density of the chemisorbed oxygen species (O_2^-), which is related to the deep oxidation of CH_4. However, the doping of metal ions (Li, Mg, Zn, Ce) is beneficial for increasing the surface oxygen species' (O_2^{2-}/O^-) density, which is crucial to improving the catalytic selectivity for C2 products. Thus, the Mg-La_2O_3 catalyst with the highest density of surface oxygen species (O_2^{2-}/O^-) shows the highest selectivity for C2 products.

The selectivity for C2 products improved by the doping of metal ions is also related to the reaction temperature. The Ce-La_2O_3 catalyst shows good catalytic selectivity for C2 products (T < 680 °C), indicating that the doping of Ce ions enhances the coupling property of the C–C bonds. It may be related to the heat released from CH_4 oxidation, which can promote the enhancement of the reaction rate of the OCM reaction [53]. Although the O1s XPS spectrum of the Ce-La_2O_3 catalyst is similar with that of the La_2O_3 catalyst, Ce-based oxide has good oxygen storage and release because of the valence alternation between Ce^{3+} and Ce^{4+} species. Thus, the Ce-La_2O_3 catalyst shows relatively high catalytic activity for the OCM reaction at low temperatures in comparison with the La_2O_3 catalyst, which is related to the Ce-sites for O_2 activation. However, with the increase in the reaction temperature, its selectivity for C2 products decreases. Thus, the effect of doped metal ions on the catalytic performance for OCM reaction has optimal reaction temperature conditions, and the doping of metal ions into La_2O_3 nanorods can promote the catalytic yield of C2 products during the OCM reaction.

3. Experimental Sections

3.1. Catalyst Preparation

For the preparation of all the catalysts in this study, the used reagents are listed in Table S1. La_2O_3 nanorods with uniform morphology were obtained by the one-pot hydrothermal method. The contrastive La_2O_3 nanoparticles were shown in Figure S2 and its catalyst performance were shown in Figure S12. The complex oxide catalyst of La_2O_3 and other metals is then prepared by adding salt solution of active metal. The schematic representation for preparing La_2O_3 catalysts includes the procedures as follows: the $La(NO_3)_3{\cdot}6H_2O$ and the corresponding metal salts (Li, Mg, Zn, Ce) were dissolved in deionized water (50 mL) to form the mixed salt solution. The theoretical doping amount of metal ions (Li, Mg, Zn, Ce) was 2 wt%. Then, the prepared NaOH solution was added to mixed salt solution drop by drop and stirred vigorously. Subsequently, the production was placed in the polytetrafluoroethylene autoclave (100 mL), which was heated at 160 °C for 12 h. The products were washed by the distilled water and ethanol, and then the $La(OH)_3$

nanorods were dried at 50 °C. After the $La(OH)_3$ nanorods were calcinated at 800 °C (maintain the La_2O_3 phase and reduce the influence of volatiles on catalytic performance) for 4 h in air, the samples of X-La_2O_3 nanorods were obtained. There was no Na1s XPS peak exhibited in the XPS survey spectrum (Figure S3), indicating that Na was completely cleaned. The catalysts were recorded as La_2O_3, Li-La_2O_3, Mg-La_2O_3, Zn-La_2O_3, and Ce-La_2O_3, respectively [21]. The synthesis diagram is shown in Figure S1.

3.2. Catalyst Characterizations

The X-ray diffraction (XRD) patterns were acquired at the scanning rate of 4° min^{-1} in the range of 5–90°. An in Via Reflex Renishaw spectrometer with the excitation wavelength of 325 nm (He-Cd laser) was used to obtain Raman spectra. The field emission high-resolution transmission electron microscope (HRTEM) was applied to observe the morphology and surface microstructure of the catalysts. The surface and pore characterizations of the catalyst were studied by the nitrogen adsorption-desorption method, which were performed on the Micromeritics ASAP 2010 automatic specific surface analyzer. The specific surface areas of the catalysts were obtained by the Brunauer–Emmett–Teller method. The temperature programmed reduction of hydrogen (H_2-TPR) reaction was used to explore their redox property. The catalysts were pretreated to remove the oxygen and other active gases adsorbed on the surface of the catalyst at 300 °C for 0.5 h in N_2. The H_2-TPR tests were performed at a rising temperature rate of 10 °C·min^{-1} in the 10% H_2/Ar. The TCD detector was used to monitor the signals of H_2 consumption [22]. X-ray photoelectron spectroscopy (XPS) was applied to determine the electronic state of each component element on the sample surface. The test instrument is produced by Perkin-Elmer, Boston, MA, USA, and the model is PHI-1600 ESCA multi-function tester. The C 1s element in the vacuum chamber is used for the binding energy (284.6 eV) of the calibration and correction of other element peaks.

3.3. Catalyst Activity Evaluation

The activity test of the catalyst was carried out using the micro fixed-bed reactor with a quartz tube (length, 450 mm; inner diameter, 6mm). The thermocouple was used to precisely control the temperature of the reaction bed (500–800 °C). The catalyst (100 mg) was applied to test the catalytic activity under the reactant gas flow (50 mL·min^{-1}, the mole ratio of O_2 to CH_4 is 1/3). The chromatograph (GC9890B, Beijing, China) with a flame ionization detector (FID) was used to test the outlet gas concentrations of CH_4, C_2H_4 and C_2H_6. The CH_4 conversion (C_{CH4}) and C_2H_4/C_2H_6 selectivity (S_{C2}) were calculated by the equations as follows.

$$\text{Conversion } (\%) = \frac{[CH_4]^0 - [CH_4]}{[CH_4]^0} \times 100$$

$$\text{Selectivity } (\%) = \frac{2[C_2H_4 + C_2H_6]}{[CH_4]^0 - [CH_4]} \times 100$$

$$\text{Yield } (\%) = \text{Conversion}(\%) \times \text{Selectivity } (\%)/100\%$$

4. Conclusions

A series of metal ion (Li, Mg, Zn, Ce)-doped La_2O_3 nanorod catalysts were successfully prepared by the hydrothermal method, which have exposed {110} crystal facets. The exposed {110} crystal facets of La_2O_3 nanorods play a crucial role in boosting the catalytic activity for OCM. The doping of metal ions can improve the redox properties of the catalyst and increase the active oxygen species amounts. X-La_2O_3 catalysts exhibit high catalytic activity and selectivity for CH_4 conversion to C2 products during the OCM reaction. Among the catalysts, the selectivity (78.4%) and yield (21%) of Mg-La_2O_3 catalysts for CH_4 conversion to C2 products are the largest. The catalytic performance of the catalyst for OCM is dependent on the doping of metal ions into La_2O_3 nanorods. The X-La_2O_3 catalysts also

exhibit high stability during the catalytic OCM reaction process. Therefore, the research results can not only provide a novel research strategy for metal-doped La-based catalysts, but can also offer a method to develop efficient catalysts for the OCM reaction.

Supplementary Materials: The following supporting information can be downloaded at: https://www.mdpi.com/article/10.3390/catal12070713/s1, Figure S1 Schematic Process for the preparation of X-La_2O_3 catalysts; Table S1 Reagents applied for preparation of catalysts; Figure S2 SEM images of pure La_2O_3 nanoparticles catalyst; Figure S3 XPS survey spectrum (0–1100 eV) of X-La_2O_3 catalysts. (A) Li-La_2O_3; (B) Mg-La_2O_3; (C) Zn-La_2O_3; (D) Ce-La_2O_3; Figure S4 TEM Images of pure La_2O_3 (a, b), Li- La_2O_3 (c) Mg-La_2O_3 (d) catalyst; Figure S5 N_2 adsorption-desorption isotherms of the La_2O_3 and X-La_2O_3 catalysts. (a) La_2O_3; (b) Li-La_2O_3; (c) Mg-La_2O_3; (d) Zn-La_2O_3; (e) Ce-La_2O_3; Figure S6 X-ray photoelectron spectra (XPS) of Li1s, Mg1s, Zn2p and Ce3d in X-La2O3 catalysts. (a) Li-La_2O_3; (b) Mg-La_2O_3; (c) Zn-La_2O_3; (d) Ce-La_2O_3; Figure S7 X-ray photoelectron spectra (XPS) of C1s over the La_2O_3 and X-La_2O_3 catalysts. (a) La_2O_3; (b) Li-La_2O_3; (c) Mg-La_2O_3; (d) Zn-La_2O_3; (e) Ce-La_2O_3; Figure S8 Stability test of the Mg-La_2O_3 catalysts for OCM; Figure S9 SEM images of Mg-La_2O_3 catalyst used for 15 h during OCM reaction; Figure S10 TEM Images of Mg-La_2O_3 catalyst used for 15 h during OCM reaction; Figure S11 The selectivity of C2 products for OCM reaction over the La_2O_3 and X-La_2O_3 catalysts; Figure S12 Catalyst performance of La_2O_3 nanoparticles catalyst.

Author Contributions: The manuscript was written through the contributions of all the authors. Conceptualization, Z.Z. and J.L.; writing—review and editing, J.X.; methodology, H.Y.; software, C.X.; formal analysis, K.L.; project administration, Y.W. All authors have read and agreed to the published version of the manuscript.

Funding: This research was funded by the National Natural Science Foundation of China (21972166), Beijing Natural Science Foundation (2202045), PetroChina Innovation Foundation (2018D-5007-0505), Science Foundation of China University of Petroleum, Beijing (No. 2462021YJRC018).

Conflicts of Interest: The authors declare no competing financial interest.

References

1. Sadjadi, S.; Jašo, S.; Godini, H.R.; Arndt, S.; Wollgarten, M.; Blume, R.; Görke, O.; Schomäcker, R.; Wozny, G.; Simon, U. Feasibility study of the Mn-Na_2WO_4/SiO_2 catalytic system for the oxidative coupling of methane in a fluidized-bed reactor. *Catal. Sci. Technol.* **2015**, *5*, 942–952. [CrossRef]
2. Hou, Y.; Han, W.; Xia, W.; Wan, H. Structure Sensitivity of $La_2O_2CO_3$ Catalysts in the Oxidative Coupling of Methane. *ACS Catal.* **2015**, *5*, 1663–1674. [CrossRef]
3. Sato, A.; Ogo, S.; Takeno, Y.; Takise, K.; Seo, J.G.; Sekine, Y. Electric Field and Mobile Oxygen Promote Low-Temperature Oxidative Coupling of Methane over $La_{1-x}Ca_xAlO_{3-x}$ Perovskite Catalysts. *ACS Omega* **2019**, *4*, 10438–10443. [CrossRef] [PubMed]
4. Zou, S.; Li, Z.; Zhou, Q.; Pan, Y.; Yuan, W.; He, L.; Wang, S.; Wen, W.; Liu, J.; Wang, Y.; et al. Surface coupling of methyl radicals for efficient low-temperature oxidative coupling of methane. *Chin. J. Catal.* **2021**, *42*, 1117–1125. [CrossRef]
5. Li, Z.; He, L.; Wang, S.; Yi, W.; Zou, S.; Xiao, L.; Fan, J. Fast Optimization of $LiMgMnO_x$/La_2O_3 Catalysts for the Oxidative Coupling of Methane. *ACS Comb. Sci.* **2017**, *19*, 15–24. [CrossRef]
6. Gambo, Y.; Jalil, A.A.; Triwahyono, S.; Abdulrasheed, A.A. Recent advances and future prospect in catalysts for oxidative coupling of methane to ethylene: A review. *J. Ind. Eng. Chem.* **2018**, *59*, 218–229. [CrossRef]
7. Ghose, R.; Hwang, H.T.; Varma, A. Oxidative coupling of methane using catalysts synthesized by solution combustion method. *Appl. Catal. A-Gen.* **2013**, *452*, 147–154. [CrossRef]
8. Song, J.; Sun, Y.; Ba, R.B.; Huang, S.; Zhao, Y.; Zhang, J.; Sun, Y.; Zhu, Y. Monodisperse Sr-La_2O_3 hybrid nanofibers for oxidative coupling of methane to synthesize C_2 hydrocarbons. *Nanoscale* **2015**, *7*, 2260–2264. [CrossRef]
9. Khodadadian, M.; Taghizadeh, M.; Hamidzadeh, M. Effects of various barium precursors and promoters on catalytic activity of Ba–Ti perovskite catalysts for oxidative coupling of methane. *Fuel. Process. Technol.* **2011**, *92*, 1164–1168. [CrossRef]
10. He, J.; Xu, T.; Wang, Z.; Zhang, Q.; Deng, W.; Wang, Y. Transformation of Methane to Propylene: A Two-Step Reaction Route Catalyzed by Modified CeO_2 Nanocrystals and Zeolites. *Angew. Chem. Int. Ed.* **2012**, *51*, 2438–2442. [CrossRef]
11. Wang, K.; Ji, S.; Shi, X.; Tang, J. Autothermal oxidative coupling of methane on the $SrCO_3$/Sm_2O_3 catalysts. *Catal. Commun.* **2009**, *10*, 807–810. [CrossRef]
12. Lei, Y.; Chu, C.; Li, S.; Sun, Y. Methane Activations by Lanthanum Oxide Clusters. *J. Phys. Chem. C* **2014**, *118*, 7932–7945. [CrossRef]
13. Sollier, B.M.; Bonne, M.; Khenoussi, N.; Michelin, L.; Miro, E.E.; Gomez, L.E.; Boix, A.V.; Lebeau, B. Synthesis and Characterization of Electrospun Nanofibers of Sr-La-Ce Oxides as Catalysts for the Oxidative Coupling of Methane. *Ind. Eng. Chem. Res.* **2020**, *59*, 11419–11430. [CrossRef]

14. Hou, S.; Cao, Y.; Xiong, W.; Liu, H.; Kou, Y. Site Requirements for the Oxidative Coupling of Methane on SiO_2-Supported Mn Catalysts. *Ind. Eng. Chem. Res.* **2006**, *45*, 7077–7083. [CrossRef]
15. Chung, E.Y.; Wang, W.K.; Nadgouda, S.G.; Baser, D.S.; Sofranko, J.A.; Fan, L. Catalytic Oxygen Carriers and Process Systems for Oxidative Coupling of Methane Using the Chemical Looping Technology. *Ind. Eng. Chem. Res.* **2016**, *55*, 12750–12764. [CrossRef]
16. Ma, X.; Sun, K.; Liu, J.; Li, W.; Cai, X.; Su, H. Single Ru Sites-Embedded Rutile TiO_2 Catalyst for Non-Oxidative Direct Conversion of Methane: A First-Principles Study. *J. Phys. Chem. C* **2019**, *123*, 14391–14397. [CrossRef]
17. Cheng, Z.; Baser, D.S.; Nadgouda, S.G.; Qin, L.; Fan, J.A.; Fan, L. C2 Selectivity Enhancement in Chemical Looping Oxidative Coupling of Methane over a Mg–Mn Composite Oxygen Carrier by Li-Doping-Induced Oxygen Vacancies. *ACS Energy Lett.* **2018**, *3*, 1730–1736. [CrossRef]
18. Kiani, D.; Sourav, S.; Baltrusaitis, J.; Wachs, I.E. Oxidative Coupling of Methane (OCM) by SiO_2-Supported Tungsten Oxide Catalysts Promoted with Mn and Na. *ACS Catal.* **2019**, *9*, 5912–5928. [CrossRef]
19. Wang, S.; Li, S.; Dixon, D.A. Mechanism of selective and complete oxidation in La_2O_3-catalyzed oxidative coupling of methane. *Catal. Sci. Technol.* **2020**, *10*, 2602–2614. [CrossRef]
20. Aljama, H.; Nørskov, J.K.; Abild-Pedersen, F. Tuning Methane Activation Chemistry on Alkaline Earth Metal Oxides by Doping. *J. Phys. Chem. C* **2018**, *122*, 22544–22548. [CrossRef]
21. Liu, W.C.; Ralston, W.T.; Melaet, G.; Somorjai, G.A. Oxidative coupling of methane (OCM): Effect of noble metal (M = Pt, Ir, Rh) doping on the performance of mesoporous silica MCF-17 supported Mn_xO_y-Na_2WO_4 catalysts. *Appl. Catal. A* **2017**, *545*, 17–23. [CrossRef]
22. Wang, Z.; Wang, D.; Gong, X. Strategies to Improve the Activity While Maintaining the Selectivity of Oxidative Coupling of Methane at La_2O_3: A Density Functional Theory Study. *ACS Catal.* **2019**, *10*, 586–594. [CrossRef]
23. Yoon, S.; Lim, S.; Choi, J.; Suh, D.J.; Song, K.H.; Ha, J. Study on the unsteady state oxidative coupling of methane: Effects of oxygen species from O_2, surface lattice oxygen, and CO_2 on the C2+ selectivity. *RSC Adv.* **2020**, *10*, 35889–35897. [CrossRef] [PubMed]
24. Chu, C.; Zhao, Y.; Li, S.; Sun, Y. Correlation between the acid-base properties of the La_2O_3 catalyst and its methane reactivity. *Phys. Chem. Chem. Phys.* **2016**, *18*, 16509–16517. [CrossRef]
25. Ferreira, V.J.; Tavares, P.; Figueiredo, J.L.; Faria, J.L. Ce-Doped La_2O_3 based catalyst for the oxidative coupling of methane. *Catal. Commun.* **2013**, *42*, 50–53. [CrossRef]
26. Kondratenko, E.V.; Schlvter, M.; Baerns, M.; Linke, D.; Holena, M. Developing catalytic materials for the oxidative coupling of methane through statistical analysis of literature data. *Catal. Sci. Technol.* **2015**, *5*, 1668–1677. [CrossRef]
27. Noon, D.; Zohour, B.; Senkan, S. Oxidative coupling of methane with La_2O_3–CeO_2 nanofiber fabrics: A reaction engineering study. *J. Nat. Gas Sci. Eng.* **2014**, *18*, 406–411. [CrossRef]
28. Shen, Y.; Zhang, Y. Transmission protocol for secure big data in two-hop wireless networks with cooperative jamming. *Inform. Sci.* **2014**, *281*, 201–210. [CrossRef]
29. Wu, Q.; Xiong, J.; Zhang, Y.; Mei, X.; Wei, Y.; Zhao, Z.; Liu, J.; Li, J. Interaction-Induced Self-Assembly of Au@La_2O_3 Core–Shell Nanoparticles on $La_2O_2CO_3$ Nanorods with Enhanced Catalytic Activity and Stability for Soot Oxidation. *ACS Catal.* **2019**, *9*, 3700–3715. [CrossRef]
30. Cui, J.; Hope, G.A. Raman and Fluorescence Spectroscopy of CeO_2, Er_2O_3, Nd_2O_3, Tm_2O_3, Yb_2O_3, La_2O_3, and Tb_4O_7. *J. Spectrosc.* **2015**, *2015*, 1–8. [CrossRef]
31. Palmer, M.S.; Neurock, M.; Olken, M.M. Periodic Density Functional Theory Study of Methane Activation over La_2O_3: Activity of O^{2-}, O^-, O_2^{2-}, Oxygen Point Defect, and Sr^{2+} Doped Surface Sites. *J. Am. Chem. Soc.* **2002**, *124*, 8452–8461. [CrossRef] [PubMed]
32. Geo, J.K.; Joshua, T.A.; Hyun, T.H. Effect of TiO_2 on the Performance of Mn/Na_2WO_4 Catalysts in Oxidative Coupling of Methane. *Ind. Eng. Chem. Res.* **2021**, *60*, 3914–3921.
33. Gao, Z.; Shi, Y. Suppressed formation of CO_2 and H_2O in the oxidative coupling of methane over La_2O_3/MgO catalyst by surface modification. *J. Nat. Gas. Chem.* **2010**, *19*, 173–178. [CrossRef]
34. Yildiz, M.; Simon, U.; Otremba, T.; Aksu, Y.; Kailasam, K.; Thomas, A.; Schomäcker, R.; Arndt, S. Support material variation for the MnxOy-Na_2WO_4/SiO_2 catalyst. *Catal. Today* **2014**, *228*, 5–14. [CrossRef]
35. Vandewalle, L.A.; Van Geem, K.M.; Marin, G.B.; Bos, R. A Boudart Number for the Assessment of Irreducible Pellet-Scale Mass Transfer Limitations: Application to Oxidative Coupling of Methane. *Ind. Eng. Chem. Res.* **2021**, *60*, 6538–6553. [CrossRef]
36. Nguyen, T.N.; Nhat, T.T.P.; Takimoto, K.; Thakur, A.; Nishimura, S.; Ohyama, J.; Miyazato, I.; Takahashi, L.; Fujima, J.; Takahashi, K.; et al. High-Throughput Experimentation and Catalyst Informatics for Oxidative Coupling of Methane. *ACS Catal.* **2019**, *10*, 921–932. [CrossRef]
37. Daneshpayeh, M.; Khodadadi, A.; Mostoufi, N.; Mortazavi, Y.; Sotudeh-Gharebagh, R.; Talebizadeh, A. Kinetic modeling of oxidative coupling of methane over Mn/Na_2WO_4/SiO_2 catalyst. *Fuel Process. Technol.* **2009**, *90*, 403–410. [CrossRef]
38. Silva, A.M.T.; Machado, B.F.; Gomes, H.T.; Figueiredo, J.L.; Dražić, G.; Faria, J.L. Pt nanoparticles supported over Ce–Ti–O: The solvothermal and photochemical approaches for the preparation of catalytic materials. *J. Nanopart. Res.* **2010**, *12*, 121–133. [CrossRef]
39. Jiang, T.; Song, J.; Huo, M.; Yang, N.; Liu, J.; Zhang, J.; Sun, Y.; Zhu, Y. La_2O_3 catalysts with diverse spatial dimensionality for oxidative coupling of methane to produce ethylene and ethane. *RSC Adv.* **2016**, *6*, 34872–34876. [CrossRef]

40. Ferreira, V.J.; Tavares, P.; Figueiredo, J.L.; Faria, J.L. Effect of Mg, Ca, and Sr on CeO_2 Based Catalysts for the Oxidative Coupling of Methane: Investigation on the Oxygen Species Responsible for Catalytic Performance. *Ind. Eng. Chem. Res.* **2012**, *51*, 10535–10541. [CrossRef]
41. Chrétien, S.; Metiu, H. Hydrogen Dissociative Adsorption on Lanthana: Polaron Formation and the Role of Acid−Base Interactions. *J. Phys. Chem. C* **2015**, *119*, 19876–19882. [CrossRef]
42. Kwapien, K.; Paier, J.; Sauer, J.; Geske, M.; Zavyalova, U.; Horn, R.; Schwach, P.; Trunschke, A.; Schlögl, R. Sites for Methane Activation on Lithium-Doped Magnesium Oxide Surfaces. *Angew. Chem. Int. Ed.* **2014**, *53*, 8774–8778. [CrossRef] [PubMed]
43. Mohammad, S.S.; Maryam, A.; Hamid, R.G.; Oliver, G.; Günter, W. Sustainable Process Design for Oxidative Coupling of Methane (OCM): Comprehensive Reactor Engineering via Computational Fluid Dynamics (CFD) Analysis of OCM Packed-Bed Membrane Reactors. *Ind. Eng. Chem. Res.* **2016**, *55*, 3287–3299.
44. Xu, J.; Zhang, Y.; Xu, X.; Fang, X.; Xi, R.; Liu, Y.; Zheng, R.; Wang, X. Constructing $La_2B_2O_7$ (B = Ti, Zr, Ce) Compounds with Three Typical Crystalline Phases for the Oxidative Coupling of Methane: The Effect of Phase Structures, Superoxide Anions, and Alkalinity on the Reactivity. *ACS Catal.* **2019**, *9*, 4030–4045.
45. Balasubramanian, R.; Smith, S.M.; Rawat, S.; Yatsunyk, L.A.; Stemmler, T.L.; Rosenzweig, A.C. Oxidation of methane by a biological dicopper centre. *Nature* **2010**, *465*, 115–119.
46. Ahari, J.S.; Ahmadi, R.; Mikami, H.; Inazu, K.; Zarrinpashne, S.; Suzuki, S.; Aika, K. Application of a simple kinetic model for the oxidative coupling of methane to the design of effective catalysts. *Catal. Today* **2009**, *145*, 45–54.
47. Aritani, H.; Yamada, H.; Nishio, T.; Shiono, T.; Imamura, S.; Kudo, M.; Hasegawa, S.; Tanaka, T.; Yoshida, S. Characterization of Li-Doped MgO Catalysts for Oxidative Coupling of Methane by Means of Mg K-Edge XANES. *J. Phys. Chem. B* **2000**, *104*, 10133–10143. [CrossRef]
48. Tang, L.; Yamaguchi, D.; Wong, L.; Burke, N.; Chiang, K. The promoting effect of ceria on Li/MgO catalysts for the oxidative coupling of methane. *Catal. Today* **2011**, *178*, 172–180.
49. Elkins, T.W.; Hagelin-Weaver, H.E. Characterization of Mn–Na_2WO_4/SiO_2 and Mn–Na_2WO_4/MgO catalysts for the oxidative coupling of methane. *Appl. Catal. A-Gen.* **2015**, *497*, 96–106. [CrossRef]
50. Gawande, M.B.; Goswami, A.; Asefa, T.; Guo, H.; Biradar, A.V.; Peng, D.; Zboril, R.; Varma, R.S. Core–shell nanoparticles: Synthesis and applications in catalysis and electrocatalysis. *Chem. Soc. Rev.* **2015**, *44*, 7540–7590. [CrossRef]
51. Schucker, R.C.; Derrickson, K.J.; Ali, A.K.; Caton, N.J. Identification of the Optimum Catalyst and Operating Conditions for Oxidative Coupling of Methane: Activity and Selectivity of Alkaline Earth-Doped Lanthanides. *Ind. Eng. Chem. Res.* **2020**, *59*, 18434–18446. [CrossRef]
52. Wang, W.; Ji, S.; Pan, D.; Li, C. A novel particle/monolithic two-stage catalyst bed reactor and their catalytic performance for oxidative coupling of methane. *Fuel Process. Technol.* **2011**, *92*, 541–546. [CrossRef]
53. Huang, P.; Zhao, Y.; Zhang, J.; Zhu, Y.; Sun, Y. Exploiting shape effects of La_2O_3 nanocatalysts for oxidative coupling of methane reaction. *Nanoscale* **2013**, *5*, 10844. [CrossRef] [PubMed]